Contents lists available at ScienceDirect

Deep-Sea Research II

Biological and physical controls on O_2/Ar, Ar and pCO_2 variability at the Western Antarctic Peninsula and in the Drake Passage

R. Eveleth [a,*], N. Cassar [a], S.C. Doney [b], D.R. Munro [c], C. Sweeney [d,e]

[a] Division of Earth and Ocean Sciences, Nicholas School of the Environment, Duke University, Durham, NC, USA
[b] Marine Chemistry and Geochemistry, Woods Hole Oceanographic Institution, Woods Hole, MA, USA
[c] Department of Atmospheric and Oceanic Sciences and Institute of Arctic and Alpine Research, University of Colorado, Boulder, CO, USA
[d] Cooperative Institute for Research in Environmental Sciences, University of Colorado, Boulder, CO, USA
[e] NOAA Earth System Research Laboratory, Boulder, CO, USA

ARTICLE INFO

ABSTRACT

Using simultaneous sub-kilometer resolution underway measurements of surface O_2/Ar, total O_2 and pCO_2 from annual austral summer surveys in 2012, 2013 and 2014, we explore the impacts of biological and physical processes on the O_2 and pCO_2 system spatial and interannual variability at the Western Antarctic Peninsula (WAP). In the WAP, mean O_2/Ar supersaturation was $(7.6 \pm 9.1)\%$ and mean pCO_2 supersaturation was $(-28 \pm 22)\%$. We see substantial spatial variability in O_2 and pCO_2 including sub-mesoscale/mesoscale variability with decorrelation length scales of ~ 4.5 km, consistent with the regional Rossby radius. This variability is embedded within onshore–offshore gradients. O_2 in the LTER grid region is driven primarily by biological processes as seen by the median ratio of the magnitude of biological oxygen (O_2/Ar) to physical oxygen (Ar) supersaturation anomalies (%) relative to atmospheric equilibrium (2.6), however physical processes have a more pronounced influence in the southern onshore region of the grid where we see active sea-ice melting. Total O_2 measurements should be interpreted with caution in regions of significant sea-ice formation and melt and glacial meltwater input. pCO_2 undersaturation predominantly reflects biological processes in the LTER grid. In contrast we compare these results to the Drake Passage where gas supersaturations vary by smaller magnitudes and decorrelate at length scales of ~ 12 km, in line with latitudinal changes in the regional Rossby radius. Here biological processes induce smaller O_2/Ar supersaturations (mean $(0.14 \pm 1.3)\%$) and pCO_2 under-saturations (mean $(-2.8 \pm 3.9)\%$) than in the WAP, and pressure changes, bubble and gas exchange fluxes drive stable Ar supersaturations.

© 2016 Elsevier Ltd All rights reserved.

1. Introduction

Rapid climate change, large uncertainty and communication with deep waters make the Southern Ocean, including productive coastal marginal ice zones such as the Western Antarctic Peninsula (WAP) and open ocean regions like the Drake Passage, a key region for the study of carbon cycling and sequestration via the biological and solubility pumps (e.g. Arrigo et al., 2008; Caldeira and Duffy, 2000). As atmospheric CO_2 levels rise and ice melts we have insufficient knowledge of how the flux of carbon between atmosphere and ocean might change. A critical component of this is our understanding of biological–physical coupling and the scales at which those processes are occurring. Dissolved gases including oxygen (O_2), argon (Ar) and carbon dioxide (CO_2) serve as valuable tools for investigating this relationship because together they record biological and physical processes at high spatial resolutions (Carrillo et al., 2004; Eveleth et al., 2014; Shadwick et al., 2015; Stanley et al., 2010; Tortell et al., 2014, 2015).

Exploiting the similar solubility properties of O_2 and argon (Ar), we isolate the biological oxygen supersaturation ($\sim\Delta(O_2/Ar)$), a record of net community production (NCP) in the mixed layer, and physical oxygen supersaturation (ΔAr), a signal of abiotic processes including those that alter solubility (e.g. temperature, salinity and atmospheric pressure changes) and change Ar concentration (e.g. bubbles, ice melt/freeze). Using Equilibrator Inlet Mass Spectrometry (EIMS) (Cassar et al., 2009) we are able to continuously measure the O_2/Ar ratio underway in the surface mixed layer at sub-kilometer resolution. As first presented in Eveleth et al. (2014), concurrent total oxygen measurements allow us to isolate Ar.

This decomposed oxygen signal can also help elucidate biotic and abiotic drivers of the CO_2 system after accounting for the differing re-equilibration time scales of O_2 (weeks) and pCO_2 (seasons–year) (Broecker and Peng, 1974). The surface water partial pressure of CO_2 (pCO_2) is controlled by sea surface temperature (SST), sea surface salinity (SSS), dissolved inorganic carbon (DIC) and alkalinity (Alk), with DIC and Alk in turn determined by air–sea gas exchange, horizontal and vertical transport, mixing and biological processes.

In this paper, we document the relative contribution of biological and physical processes to the total O_2 and pCO_2 signals recorded at the WAP and assess the magnitude and spatial scales of variability to inform our understanding of these processes and how best to sample them. Additionally, we compare dynamics in the WAP with open ocean conditions in the Drake Passage. While others have addressed the relative roles of biological and physical processes on the O_2, pCO_2 and dissolved inorganic carbon systems of the Southern Ocean (Carrillo et al., 2004; Hauri et al., 2015; Shadwick et al., 2015; Tortell et al., 2015), here we additionally investigate the interannual variability in these signals and quantify physical contributions. In a companion paper (Eveleth et al., 2017b), we use these underway O_2/Ar and pCO_2 measurements to estimate NCP in the WAP and subsequently detail the mechanisms and limiting factors controlling the biological variability that we expose in this first paper. The companion paper focuses on the role of glacial and sea-ice meltwater as they relate to iron and light availability.

2. Methods

Underway measurements were collected onboard the ARSV *Laurence M. Gould* (LMG) during the austral summer (January–early February) 2012, 2013 and 2014 in conjunction with the Palmer Long-Term Ecological Research Project (LTER) annual cruise which occupies a ~ 700 km $\times$ 250 km sampling grid along the WAP typically with discrete sampling every 20–100 km along gridlines that run perpendicular to the coast (Fig. 1). Conductivity–temperature–depth (CTD) casts were taken at each discrete station with a SeaBird 911plus instrument (temperature sensor model 3plus with accuracy ± 0.001 °C, conductivity sensor model 4C with accuracy ± 0.002 S/m). Mixed layer depth was defined as the depth at which the density increased 0.125 kg m^{-3} relative to the surface. Meteoric water and sea-ice meltwater estimates were completed at each station using the $\delta^{18}O$ approach as detailed in Meredith et al. (2013). Briefly, discrete water samples were analyzed at the the Natural Environment Research Council Isotope Geochemistry Laboratory (NIGL) for $\delta^{18}O$ on a VG Isoprep 18 and SIRA 10 mass spectrometer, and these data were used with salinity to determine a three end-member mass balance that quantifies fractions of circumpolar deep water, sea-ice melt and meteoric water. Temperature and salinity were measured continuously underway from a thermosalinograph (SBE 45 MicroTSG accuracy ± 0.0003 S/m, ± 0.002 °C) at 5 m depth. These values are reported as 2-min averages and referred to as sea surface properties (SST and SSS respectively).

O_2/Ar measurements were taken using equilibrator inlet mass spectrometry (EIMS) in which seawater from the ship's underway flow-through system is pumped through a gas–permeable membrane contactor cartridge (MicroModule® 0.75 $\times$ 1) allowing gases in the headspace of the cartridge to equilibrate with gases in seawater, and the air is sent via a fused silica capillary to a quadrupole mass spectrometer (Pfeiffer Prisma model QMG 220 M1) to measure the ratio of O_2 to Ar and other dissolved gases. The system calibrates by sampling the atmosphere for 20 min every 4 h. Atmospheric O_2/Ar is very stable and there is no observable

instrument drift; the average difference between consecutive air calibrations was 0.2%. The instrument precision is $\pm 0.3\%$ or better and the EIMS e-folding response time is 7.75 ± 0.25 min (Cassar et al., 2009). We present 2-min averages of continuous underway data collected every 8 s in the surface mixed layer.

Concurrent optode measurements of total O_2 concentration were collected using an Aanderaa Optode Model 4835 (precision ± 0.2 μM). In 2012, Winkler titrations were completed at 19 discrete stations allowing calibration of the surface dissolved O_2 at 59 surface CTD stations (mean value from two optodes mounted on the CTD rosette) via a model II least-squares regression. Underway optode measurements (every 30 s) were then fit to these corrected discrete measurements (Fig. S1). While the root mean squared error of this fit is 10.1 μM, we observe no significant drift in the fit over time, and the scatter can likely be attributed to some temporal and spatial incoherence of the optode, Winkler titrations and CTD measurement matches, which is difficult to avoid. Oxygen depletion in the underway lines of the ship is likely negligible here as Winkler titration comparisons of bottle and underway samples on the LMG show a mean difference of 0.06% ($n=9$). Additionally, Juranek et al. (2010) show that the respiration effect is low (0.5% or less) at low temperatures and the distance from the seawater intake to the sampling sink is quite short so water residence time in the lines of the LMG is approximately one minute. Total O_2 and O_2/Ar measurements were averaged in 8-min bins to account for differing response times of the optode (sensor response time < 25 s) and EIMS, and ΔAr was then derived as in Eveleth et al. (2014) using

$$\Delta Ar = \frac{\Delta(O_2)_{total} + 1}{(1 + \Delta(O_2/Ar))} - 1 \tag{1}$$

where ΔAr is equal to the physical oxygen supersaturation (alternatively $[Ar]/[Ar]_{sat} - 1$), $\Delta(O_2)_{total}$ is the total O_2 supersaturation ($[O_2]/[O_2]_{sat} - 1$) and

$$\Delta(O_2/Ar) = \left[\frac{([O_2]/[Ar])}{([O_2]/[Ar])_{sat}} - 1 \right]. \tag{2}$$

$\Delta(O_2/Ar)$ is generally accepted to approximate the biological oxygen supersaturation especially as $[Ar]/[Ar]_{sat}$ approaches 1 (Cassar et al., 2011). We measure $\Delta(O_2/Ar)$ using EIMS, total O_2 concentration ($[O_2]$) with an Optode, and calculate equilibrium saturation concentrations of O_2 ($[O_2]_{sat}$, $< \pm 0.3\%$) and Ar ($[Ar]_{sat}$, $\pm 0.13\%$) using underway temperature and salinity and the equations of Garcia and Gordon (1992) and Hamme and Emerson (2004), respectively. Saturation concentrations were corrected for atmospheric pressure history as in Shadwick et al. (2015) by multiplying saturations by the ratio of the weighted sea level pressure history (NCEP/NCAR Reanalysis daily average surface level pressure, http://www.esrl.noaa.gov/psd/) to standard pressure. This allows us to solve for physical oxygen supersaturation, ΔAr. Ar supersaturations are pressure history corrected unless otherwise noted; in discussion of variability and relative contributions of biological and physical processes to total oxygen supersaturation, we use pre-pressure corrected ΔAr so as to include all physical influences. ΔAr is only available for 2012 at this time due to the lack of Winkler titrations in 2013 and 2014 and resultant inability to calibrate the Optode.

pCO_{2meas} was measured every 2.5 min (the approximate integration time of the equilibration system) using a 30 l shower-type air–water equilibrator and an IR CO_2 analyzer; analytical precision for pCO_{2meas} was estimated to be approximately ± 1.5 μatm due mostly to uncertainty in equilibration temperature, and pCO_{2atm} is estimated to be ± 0.2 μatm (Munro et al., 2015). pCO_2
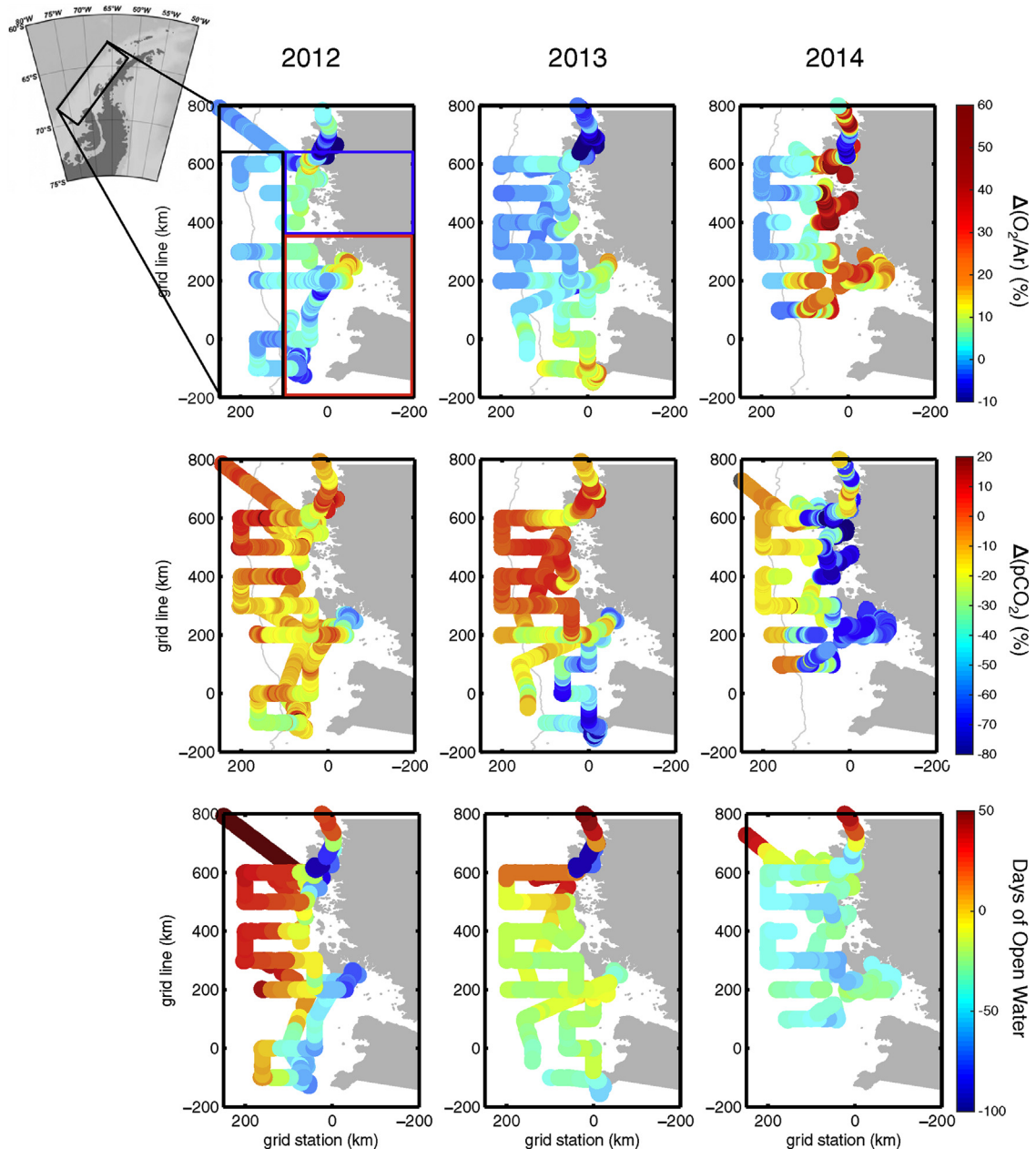
Fig. 1. $\Delta(O_2/Ar)$ (top), $\Delta(pCO_2)$ (center) and days of open water prior to ship occupation (bottom) mapped in the LTER grid region in January–early February 2012 (left), 2013 (middle) and 2014 (right). Top left map indicates offshore (black), northern onshore (blue) and southern onshore (red) grid regions. Open water is defined as $< 15\%$ ice cover and negative days of open water values indicate $> 15\%$ ice cover persistence after sampling. $\Delta(pCO_2)$ uncertainty is $\pm 0.45\%$, and $\Delta(O_2/Ar) \pm 0.3\%$. (For interpretation of the references to color in this figure legend, the reader is referred to the web version of this article.)

supersaturation ($\Delta(pCO_2)$) was calculated using the equation:

$$\Delta(pCO_2) = \left(\frac{pCO_{2\,meas}}{pCO_{2\,atm}} - 1 \right) \qquad (3)$$

where the pCO_{2atm} was taken as the cruise mean value (388 μatm 2012, 391 μatm 2013, 393 μatm 2014). Data were 4-min-averaged and time merged with all other variables. $\Delta(Ar)$, $\Delta(O_2/Ar)$ and $\Delta(pCO_2)$ are typically expressed as a percent by multiplying by 100, thus with Δ equal to 0 at equilibrium saturation. Error in gas supersaturation was estimated from standard propagation summation in quadrature assuming to first approximation that properties are normally distributed and independent. $\Delta(pCO_2)$ uncertainty is $\pm 0.45\%$, $\Delta(O_2/Ar) \pm 0.3\%$ (Cassar et al., 2009), and $\Delta(Ar)$ $\pm 0.47\%$. Gas saturations are not corrected for vertical mixing, gas exchange or advection as discussed below.

Several pre-processing steps were performed for evaluation of decorrelation length scales of underway data. For each gridline of data, discrete sections were isolated that had fewer than 5% missing data points in 50-point continuous series ($\sim$30 km). Sections rather than full gridlines were used in variability analyses to prevent issues with smoothing over frequent data gaps. Cumulative distance series were calculated for each section by finding the distance between consecutive points based on latitude and longitude and adding these distances cumulatively. All data collected when the ship was moving slower than 2 knots were discarded to prevent both effects of ship-induced mixing and aliasing when the ship was held on station. Data were then fitted using a shape-preserving piecewise cubic interpolation with 0.1 km spacing to resolve high frequency variability. Data were then subsampled at 1 km resolution consistent with measurement

frequency. Each gridline of data was then detrended to remove the best linear fit, and decorrelation length scale was determined for each 50-point subsection.

3. Results and discussion

In the following two subsections we discuss the data collected within the Palmer-LTER grid region off the WAP (Fig. 1, south of 600 km gridline). In Section 3.4 we compare grid observations to those made in Drake Passage defined here as between 55S and 63S latitude.

3.1. Overall patterns

$\Delta(O_2/Ar)$ and $\Delta(pCO_2)$ displayed strong spatial and interannual variability, with $\Delta(O_2/Ar)$ ranging from -10.5% to $+50.3\%$ and $\Delta(pCO_2)$ ranging from -86.2% to $+20.0\%$ (pCO_2 54.4–466.2 µatm) over the 3 years of sampling (Fig. 1). Overall we document summertime net autotrophic conditions in the WAP (Table 1). $\Delta(O_2/Ar)$ was $(4.2 \pm 4.7)\%$ in 2012, $(5.9 \pm 7.1)\%$ in 2013, and $(16.0 \pm 13.4)\%$ in 2014 (values quoted being mean $\pm 1\sigma$). $\Delta(O_2/Ar)$ in 2012 and 2013 were comparable to previous discrete summer measurements in the LTER region (Huang et al., 2012) and underway measurements in the ice-influenced regions of the Bellingshausen Sea in March 2007 (Castro-Morales et al., 2013), while 2014 saw anomalously high values. Some variability in the presented means could arise because of differing cruise tracks in each year (e.g., spending more or less time within highly-productive regions such as Marguerite Bay (~gridline 100–250 km, grid station -150–0 km, Fig. 1) but 2014 was abnormally productive regardless of this consideration based on averaging values only at a subset of stations common to each year (subset $\Delta(O_2/Ar)$ average $(3.9 \pm 2.7)\%$ in 2012, $(1.2 \pm 1.2)\%$ in 2013, and $(8.1 \pm 11.1)\%$ in 2014). Mean $\Delta(pCO_2)$ and surface ocean pCO_2 were $(-17.0 \pm 13.2)\%$ $(322.4 \pm 51.3$ µatm) in 2012, $(-25.6 \pm 20.9)\%$ $(287.5 \pm 83.3$ µatm) in 2013, and $(-46.4 \pm 22.0)\%$ $(221.3 \pm 91.2$ µatm) in 2014, respectively. It is difficult to say how much of the observed interannual variability in $\Delta(O_2/Ar)$ and $\Delta(pCO_2)$ is due to sampling timing relative to peak bloom conditions and how much can be attributed to absolute interannual differences in summer production. However, O_2–residence-time-integrated NCP derived from O_2/Ar is strongly correlated ($r^2 = 0.82$) with November–January NCP inventories derived from DIC drawdown with all three years displaying the same slope (0.37) suggesting that O_2/Ar is at least representing true interannual variability in Nov–Jan NCP. Both $\Delta(O_2/Ar)$ and $\Delta(pCO_2)$ display onshore–offshore gradients with strongest O_2/Ar supersaturations and pCO_2 undersaturations in the coastal onshore waters. Large O_2/Ar supersaturations are coincident with canyon locations potentially due to the role of canyon-steered upper circumpolar deep water (UCDW) onto the shelf that impacts micro-nutrient delivery and water column stability (Kavanaugh et al., 2015; Schofield et al., 2013). Biological production was

anomalously high in 2014 likely owing to late sea ice retreat and strong surface stratification (see discussion of O_2/Ar-derived NCP estimates and driving mechanisms in companion paper (Eveleth et al., 2017b)).

$\Delta(Ar)$ in 2012 ranged from -5.8% to 6.0% ($\mu \pm 2\sigma$) with a mean of $(0.2 \pm 2.9)\%$ (SE 0.02%) in 2012 (Fig. 2). This range is comparable to $\Delta(Ar)$ documented in the mixed layer in other ice influenced regions such as the upper Arctic Ocean (Eveleth et al., 2014) and Australian sector of the Southern Ocean (Shadwick et al., 2015). $\Delta(Ar)$ has a strong north–south gradient in the LTER grid region with predominant Ar undersaturations south of the 200 gridline and supersaturations to the north (Fig. 2a).

3.2. Biological vs. physical drivers of O_2, Ar, and CO_2 saturation states

Overall in the WAP region, the median ratio of the absolute value of $\Delta(O_2/Ar)$ to $\Delta(Ar)$ (pre-pressure corrected so as to include all physical processes) in 2012 is 2.6 suggesting the total O_2 signal is driven primarily by biological processes with secondary controls by physical processes (Fig. S2). The relative contributions of $\Delta(O_2/Ar)$ and $\Delta(Ar)$ to $\Delta(O_2)_{total}$ vary within the grid region. Offshore (west of grid station 100 km) $\Delta(O_2)_{total}$ is small with low positive $\Delta(O_2/Ar)$ and weak Ar undersaturations. In the northern onshore region (north of gridline 350 km and east of grid station 100 km) median $\Delta(O_2)_{total}$ is the greatest with positive $\Delta(O_2/Ar)$ and small contributions from weakly positive $\Delta(Ar)$ (i.e., $\Delta(O_2/Ar) \sim = \Delta(O_2)_{total}$). In the southern onshore region (south of gridline 350 km and east of grid station 100 km) we observe the greatest contribution of Ar undersaturation, particularly in the southeastern most corner of the grid. These drive the median $\Delta(O_2)_{total}$ down despite high positive biological contributions (i.e., $\Delta(O_2/Ar) > \Delta(O_2)_{total}$). The complex interplay of biological and physical processes influencing O_2 in ice-influenced regions make it difficult to quantitatively divide total O_2 observations (e.g. as would be obtained from underwater gliders or Bio-Argo profiling floats) into its components, but a qualitative assessment is important to consider in interpretation of O_2 measurements because physical oxygen can deviate significantly from equilibrium saturation as a result of ice processes. Notably, the Ar supersaturations presented here have already accounted for pressure history influences on solubility, and this correction should be employed in total O_2 studies as well. Time derivatives of total O_2 may be easier to interpret.

3.2.1. Drivers of Ar saturation state in 2012

Ar undersaturation was strongest in the southern onshore region and could potentially be a result of rapid cooling, freshening, and/or Ar concentration dilution from sea-ice meltwater input and/or glacial meltwater input. Supersaturation was most prominent in the northern onshore region of the LTER grid and could be driven by warming, increasing salinity, bubble processes (e.g. wave induced bubble injection or exchange) and/or mixing of two different temperature water masses. In order to produce deviations from saturation these mechanisms must act on timescales

Table 1

$\Delta(O_2/Ar)$, $\Delta(pCO_2)$ and $\Delta(Ar)$ regional means (± 1 standard deviation) for 2012, 2013, and 2014.

$\mu \pm 1\sigma$		$\Delta(O_2/Ar)$ (%)			$\Delta(pCO_2)$ (%)			ΔAr (%)
Area		2012	2013	2014	2012	2013	2014	2012
LTER grid		4.2 ± 4.7	6.0 ± 7.0	13.3 ± 12.0	-17 ± 13.2	-26.4 ± 21.3	-43.7 ± 23.2	0.2 ± 2.9
N Onshore		6.7 ± 5.2	0.4 ± 2.4	25.6 ± 13.9	-14.7 ± 8.6	-7.4 ± 10.2	-58.5 ± 18.1	1.8 ± 1.5
S Onshore		4.4 ± 4.8	9.5 ± 7.1	14.6 ± 7.8	-20 ± 13.7	-39.2 ± 17.1	-53.5 ± 13.1	-0.2 ± 3.3
Offshore		1.3 ± 1.2	0.9 ± 1.5	1.64 ± 2.4	-8 ± 9.4	-7.9 ± 9.6	-13.4 ± 8.3	0.5 ± 1.3
DP	**NPF**	0.1 ± 0.2	1.8 ± 1.9	2.7 ± 0.8	-2.7 ± 4.0	-5.5 ± 5.4	-8.5 ± 2.3	1.5 ± 0.5
DP	**SPF**	0.0 ± 0.3	0.4 ± 0.6	1.4 ± 0.9	0.1 ± 2.4	-1.7 ± 2.9	-5.7 ± 1.8	1.2 ± 0.9

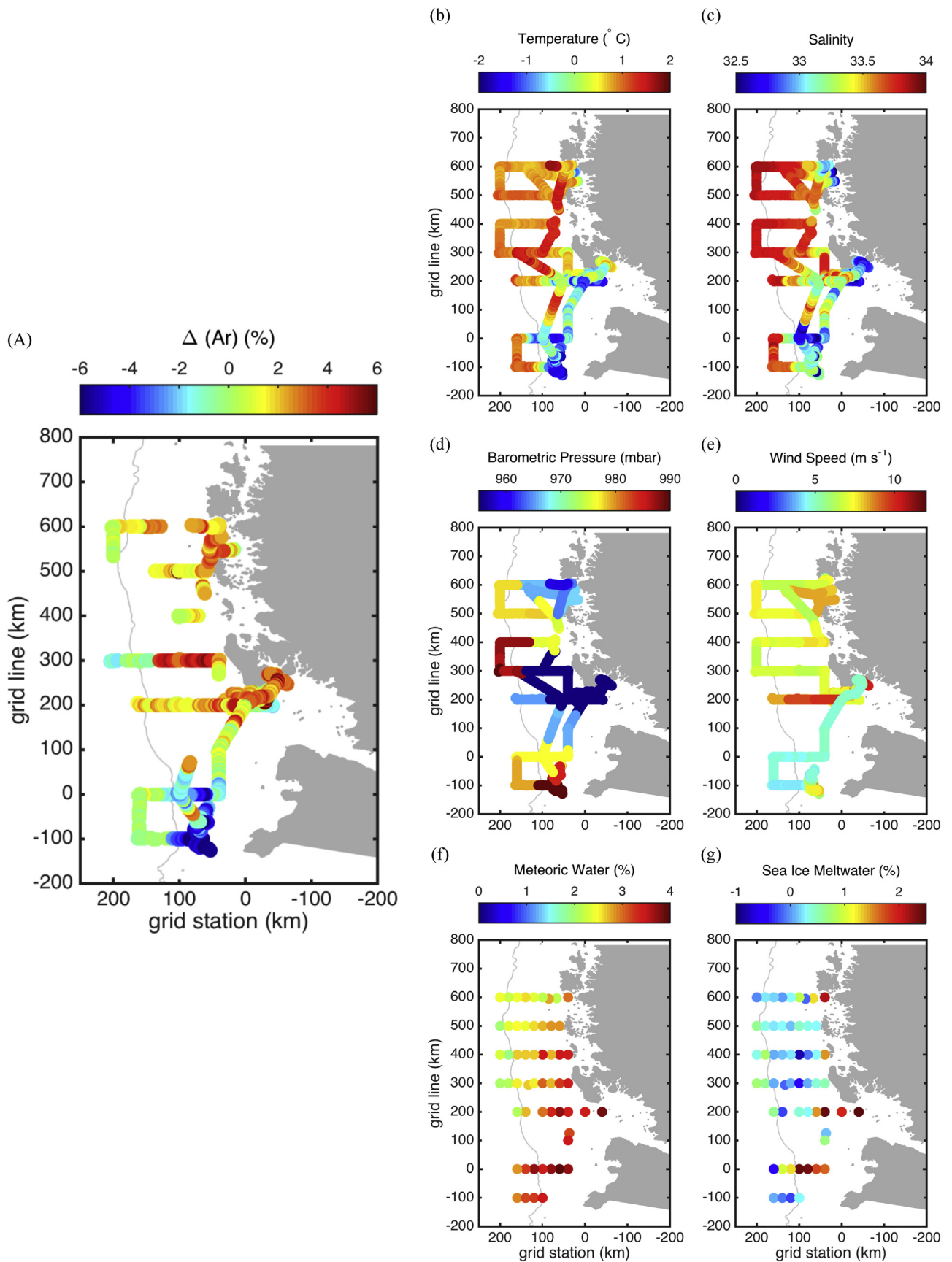**Fig. 2.** Grid maps of: (a) Δ(Ar) (uncertainty ± 0.47%) compared to potential saturation state controls, (b) SST, (c) SSS, (d) weighted barometric pressure, (e) weighted wind speed history prior to ship occupation, (f) surface meteoric water fraction, and (g) surface sea–ice meltwater fraction in 2012.

comparable to or faster than gas exchange is able to return surface waters to equilibrium with the atmosphere. We assess the likelihood, including consideration of these timescales, of each mechanism's responsibility in determining the Ar saturation state, keeping in mind some processes will work in opposite directions on supersaturation.

Spatial coherence of temperature, salinity and meltwater patterns with $\Delta(Ar)$ are shown in Fig. 2, with higher temperatures, higher salinity and low meltwater content largely associated with Ar supersaturations in the northern two-thirds of the grid region. Ice retreats from north to south along the peninsula likely contributing to the gradients in temperature, salinity and sea ice meltwater content at the time of LTER sampling. According to GSFC Bootstrap SMMR-SSM/I sea ice data (http://nsidc.org/data/nsidc-0079.html) the date of ice retreat was no more than 36 days prior to ship occupation in 2012 so the warming likely occurred within ~1 month prior to sampling. The maximum temperature and salinity changes in the season can be bounded by the observed summer mixed layer T–S characteristics compared to winter water ($-1.86\,°C$, 33.88 (Martinson et al., 2008)) (see salinity discussion below). Maximum warming observed was 3.6 °C. This warming alone could create a 9.43% Ar supersaturation if the temperature change occurred much faster than gas exchange was able to re-equilibrate the water. Median warming in the region over the month was 1.8 °C and could create a supersaturation of 5% if that change occurred rapidly prior to Ar sampling. This bound implies that the scales of warming in the region are consistent with the observed Ar supersaturations. Observed $\Delta(Ar)$ displays a linear relationship with seasonal warming (least-squares regression $n=2408$, $r^2=0.35$, $p < 0.00001$) with a slope of 3.1% Ar supersaturation per degree of warming. This is slightly higher than the expected slope of ~2.6% based on solubility changes at these low temperatures (Hamme and Emerson, 2004) likely because of compounding meltwater influences on the relationship; freshening and dilution accompany low temperatures here, which will create stronger undersaturations. Despite relatively high meltwater contributions and high variability in the biological and physical systems, local warming in Marguerite Bay is consistent with the regions of positive $\Delta(Ar)$ (2.5 °C warming coincident with up to 5% Ar supersaturation). Overall the linear relationship suggests that warming is a primary driver of observed Ar supersaturations in summer 2012.

Bubble processes may play a secondary role in creating Ar supersaturation as has been documented in several other systems (e.g. Hamme and Emerson, 2002). When waves break they force air bubbles into the water where they are then subject to increased hydrostatic pressure; bubbles act to elevate surface gas supersaturation through injection (small bubble bursting) or exchange (diffusion across the surface of a large bubble) processes. We estimated the total bubble flux using the bubble injection flux equation of Stanley et al. (2009) and assuming a 2:1 ratio of bubble injection flux: bubble exchange flux (Hamme and Emerson, 2006; Loose and Jenkins, 2014; Stanley et al., 2006). Assuming steady state and accounting for bubble flux and diffusive gas exchange, the average conditions in the WAP in 2012 (20 m MLD, 7 m s^{-1} weighted wind speed, 2.8 m d^{-1} weighted piston velocity, temperature -0.1 °C and salinity of 33.3) would induce an Ar supersaturation of ~1.0%. The total air–sea gas flux (diffusive gas exchange plus total bubble flux) is relatively small compared to solubility generated saturation state changes from warming.

Maximum seasonal freshening (calculated by comparing winter water to surface water salinity (Fig. 2c) as described above) in the WAP was a -3.3 change in surface salinity in 2012 and this freshening could create a -2.5% Ar undersaturation if the change occurred within the residence time of Ar (mixed layer depth/piston velocity). This bound implies that freshening effects on

solubility alone (not including Ar concentration dilution processes) cannot have been the sole driver of negative $\Delta(Ar)$, which reaches undersaturations of -5.8%, however this is likely a major contributor. Salinity is driven by precipitation, glacial meltwater and sea-ice meltwater in the WAP. Orographically enhanced coastal precipitation in the region (Meredith et al., 2013) would drive Ar undersaturating freshening, but this effect would likely be minimal because average 7-day precipitation in the region is ~19 mm (Meredith et al., 2013) resulting in a negligible salinity change during the residence time of Ar.

Meteoric water content based on $\delta^{18}O$ and salinity (Meredith et al., 2017) reveals strongest meteoric inputs in the southern onshore region of the grid, reflecting the coastal discharge of the glaciers and topographically-influenced precipitation. Sea-ice meltwater shows some nearshore enhancement, though with a minimum in the mid-shelf region across the central part of the grid, and a greater degree of spatial heterogeneity than for meteoric water. These patterns are generally consistent with Ar undersaturation in 2012 (Fig. 2f and g).

Glacial meltwater input at depth has recently been shown to have an overall undersaturating effect on Ar with 1% glacial meltwater input decreasing $\Delta(Ar)$ by 0.5% as a result of freshening and latent heat consumption despite Ar concentration increasing with the meltwater addition (Loose and Jenkins, 2014). Meteoric water as presented in Fig. 2f includes precipitation and has a much longer residence time than Ar (months-years vs. one week), so here we rely on glacial discharge estimates to set bounds on the strength of this driver. Meredith et al. (2013) estimate that the mean steady-state rate of glacial discharge to the Pal-LTER grid region is 55 mm month^{-1}. Assuming this rate applies in 2012, 14 mm of glacial discharge may have been added over the ~7-day open water residence time of Ar. Average MLD in the southern onshore region in 2012 was 22 ± 13 m, therefore this discharge would lead to 0.04–0.15% glacial meltwater content and a negligible ($< 0.075\%$) impact on Ar undersaturation if we linearly extrapolate the relationship of Loose and Jenkins (2014).

This approximation assumes that all bubbles in the glacial input dissolve into the water at depth and the net result is a balance of freshening, cooling and bubble addition. The nature of glacial meltwater input is not certain in this region (e.g. surface, sub-glacial, iceberg calving) at this time (Meredith et al., 2017). The method of input affects resultant gas supersaturation; if meltwater at the glacial surface has already equilibrated with the atmosphere prior to input then there will be a salinity impact but no clear Ar concentration dilution (Beaird et al., 2015) or alternatively if Ar containing air bubbles escape to the atmosphere prior to melting without time for meltwater to equilibrate, the result could be even stronger Ar undersaturation. While more study is needed on the relationship between glacial meltwater and gasses, it is unlikely that the regional discharge during the residence time of Ar could be driving significant $\Delta(Ar)$ change in the WAP.

Sea-ice melt can also drive strong Ar undersaturations. When sea ice freezes, Ar is excluded from the ice matrix and ~45% is rejected into the underlying water column (Top et al., 1988). The remaining Ar in the ice is forced into brine channels/pockets and bubbles, which escape as ice ages and melts throughout the summer (Hood, 1998). As a lower bound we first assume that sea-ice meltwater is 45% Ar undersaturated, but we note that Zhou et al. (2013) found ~-80% ΔAr for late season sea ice in the Arctic and meltwater could theoretically have an Ar concentration of zero if all brine and bubble Ar has escaped prior to melt. Summer melt creates surface water Ar undersaturations primarily via Ar concentration dilution. Melt also freshens the mixed layer amplifying the undersaturating effect. The maximum sea-ice meltwater content observed in the southern onshore region was 2.5% (Fig. 2g, Meredith et al., 2017). If we employ a mass balance with a gas-

equilibrated mixed layer and 45% Ar undersaturated meltwater added during the residence time of Ar, a 2.5% sea-ice melt fraction as locally observed in 2012 could drive a -1.6% Ar undersaturation due to the concentration change and freshening. If the meltwater had an Ar concentration of 0 and was well mixed throughout the mixed layer, the resulting undersaturation would be -3%. This serves as a maximum bound for the sea-ice melt affect on Ar here as Ar is actively re-equilibrating with the atmosphere and melt input is likely distributed over the spring and summer melt seasons, though more closely timed with ship sampling in the southern portion of the grid in 2012 (Fig. 1). We document a small area in the southeastern corner of the grid where Ar was undersaturated more than -8% in 2012. This is concurrent with salinities reaching as low as 30.6. Sea-ice meltwater data are not available here, but based on a simple mass balance assuming that the surface salinity was initially 33.88, sea-ice meltwater salinity was 7 and all freshening was a result of sea-ice melt, a 12% meltwater fraction would be needed to produce the observed seasonal freshening. A 12% sea ice meltwater fraction, such as in a recent freshwater lens, could create -14.5% Ar undersaturations and explain the extreme values observed.

3.2.2. Drivers of O_2 and pCO_2 saturation states

The buildup of biological O_2 is strongly associated with pCO_2 undersaturations (Fig. 3) as expected for a pCO_2 system being driven by biological processes consistent with previous studies of O_2 and pCO_2 in the sea-ice zone (Carrillo et al., 2004; Mu et al., 2014; Tortell et al., 2014, 2015; Tortell and Long, 2009). This is shown in the model II regression (geometric mean) of $\Delta(O_2/Ar)$ vs. $\Delta(pCO_2)$ (slope -0.39, $r^2 = 0.53$ in 2012, slope -0.34, $r^2 = 0.62$ in

2013, slope -0.56, $r^2 = 0.75$ in 2014, Fig. 3) in the peninsula region. This is broadly consistent with Carrillo et al. (2004) who found a slope of -0.4 in their comparison of summertime $\Delta(O_2)$ and $\Delta(pCO_2)$ in the WAP in 1997. The theoretical slope of this relationship if controlled entirely by biological production, and excluding air–sea gas flux, would be ~ -0.8 if we calculate it as in Carrillo et al. (2004) using a photosynthetic quotient of 1.3, a Revelle factor of 14, atmospheric CO_2 390 µatm (mean for 2012–2014 cruises), and $[O_2]_{sat}$ 350 µmol kg^{-1} (oxygen solubility from typical summertime WAP SST and SSS). The discrepancy between the theoretical and observed slopes can likely be explained by differential gas exchange as O_2 is re-equilibrated with the atmosphere much faster than pCO_2 (Carrillo et al., 2004; Tortell et al., 2015). Nonlinearity in this relationship is expected and arises due to a slow residence time for pCO_2 (months-year) relative to O_2 as well as carbonate chemistry effects resulting from a variable Revelle factor with biological productivity.

Warming (freshening) would lead to super(under) saturation in pCO_2. Significant sea surface warming above freezing temperature (-1.8 °C) does not occur in the WAP until sea ice retreats. Days of open water prior to sampling varied spatially and interannually from 36 days to -85 days, with negative values indicating that ice cover was still $> 15\%$ for that many days after sampling (Fig. 1). Retreat occurred at most 36 days prior to ship occupation, thus we can set bounds on the maximum temperature change that occurred during the residence time of pCO_2 and estimate its impact on observed pCO_2 supersaturations as done above with $\Delta(Ar)$. Re-equilibration of pCO_2 with the atmosphere is likely of secondary importance over these timescales. Using the thermodynamic relationship of Takahashi et al. (1993), considering a maximum
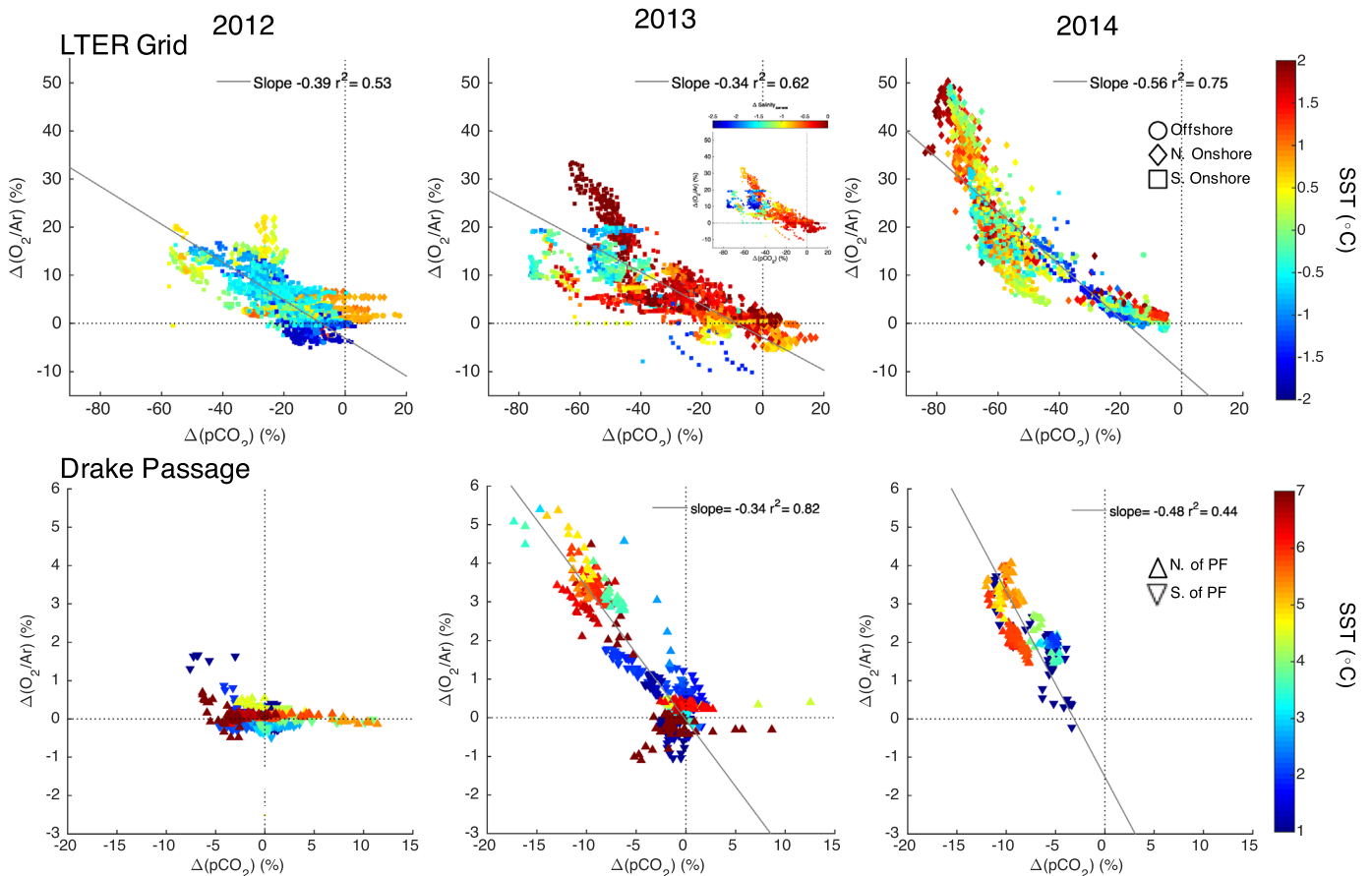

Fig. 3. $\Delta(O_2/Ar)$ vs. $\Delta(pCO_2)$ colored by SST in 2012 (left), 2013 (middle) and 2014 (right) in the LTER Grid (top) and Drake Passage (bottom). Inset in top center colored by ΔS_{sw-ww}. Symbol shape by region with circles: offshore, diamonds: northern onshore, squares: southern onshore, upward pointing triangles: North of the Polar Front (~ 58.5°S) and downward pointing triangles: South of the Polar Front. $\Delta(pCO_2)$ uncertainty is $\pm 0.45\%$, and $\Delta(O_2/Ar) \pm 0.3\%$.

seasonal warming (temperature difference between summer water and winter water, ΔT_{sw-ww}) of 3.6 °C in 2012, 5.0 °C in 2013 and 4.6 °C in 2014 the warming effect could create maximum pCO_2 supersaturations of 15% in 2012, 21% in 2013 and 20% in 2014. We do not observe a correlation between $\Delta(pCO_2)$ and ΔT_{sw-ww} in any year. On average, warming increases pCO_2 by a mean of 39 μatm ($\sim 10\%$ $\Delta(pCO_2)$) in the WAP summer. Therefore, temperature change partially offsets the $\Delta(pCO_2)$ undersaturations observed in the WAP during each year of the study but does not appear to be a dominant control on $\Delta(pCO_2)$ variability across the grid.

In 2012 and 2013 $\Delta(pCO_2)$ and salinity are correlated (model II linear regression, $r^2=0.35$, $r^2=0.42$, respectively, not shown). There are several ways in which freshening in the WAP is related to negative $\Delta(pCO_2)$ including biological drawdown in ice-edge blooms, changing solubility and DIC dilution from sea-ice and glacial meltwater freshening. The change in pCO_2 ($dpCO_2$) due to freshening is estimated as in *Takahashi* et al. (1993) by

$$dpCO_2 = \frac{pCO_{2atm} * \text{Salinity Factor}}{S}\Delta S_{sw-ww} \qquad (4)$$

where we use a salinity factor of 1.7 which is consistent with the mean, high-latitude salinity dependence, alkalinity factor and Revelle factor and includes salinity impacts on dissociation constants and changes in DIC and Alkalinity (Sarmiento and Gruber, 2006). ΔS_{sw-ww} is the seasonal freshening relative to winter water salinity (33.8 (Martinson et al., 2008)). The maximum freshening observed in each year could drive pCO_2 undersaturations of -16.4% in 2012, -12.8% in 2013 and -19.3% in 2014. Since $\Delta(O_2/Ar)$ is not affected by physical processes, this change in $\Delta(pCO_2)$ would reduce the ratio of $\Delta(O_2/Ar)$ to $\Delta(pCO_2)$ (i.e. the slope of the samples' alignment in Fig. 3). The effect of salinity is apparent in 2013 as low salinity water in the southern onshore region appears to be driving anomalously low $\Delta(pCO_2)$. The net effect of

freshening and warming is supersaturating ((4.7 ± 5.5)% in 2012; (8.4 ± 6.3)% in 2013; (3.4 ± 4.6)% in 2014) in the LTER grid. The freshening signal's undersaturating magnitude is overwhelmed by the simultaneous warming signal, but still appears to contribute to summertime $\Delta(pCO_2)$ variability in the WAP.

3.3. Variability

Strong spatial variability appears to be masking any potential diurnal cycle in $\Delta(O_2/Ar)$ and $\Delta(pCO_2)$ such as are observed in stationary time series observations at Palmer Station by Tortell et al. (2014) or during Lagrangian studies in other regions of the Southern Ocean (Hamme et al., 2012; Martin et al., 2013). Our shipboard measurements show no apparent relationship with time of day as additionally verified by the autocorrelation function of $\Delta(O_2/Ar)$ (Fig. S3).

To assess spatial variability we consider both the magnitude and spatial scales. The coefficient of variation (CV; standard deviation/mean) allows comparison of the magnitude of variability for properties with different units. We use (O_2/Ar) and (Ar) saturation ($\Delta + 100\%$) rather than supersaturation, to eliminate the possibility of a zero mean. Pre-pressure history corrected Ar saturation is used here so as to include all influences on Ar supersaturation (physical oxygen) in consideration of variability. Temperature and salinity were used to calculate oxygen solubility using the equations of Garcia and Gordon (1992) where the CV of solubility reflects the gas-relevant variation in physical properties measured underway. By binning the data into 50 km grid station windows we can additionally assess how the magnitude of variability changes from onshore (-50 to 0 km grid stations) to offshore (150–200 km grid stations) for each property, each year (Fig. 4).
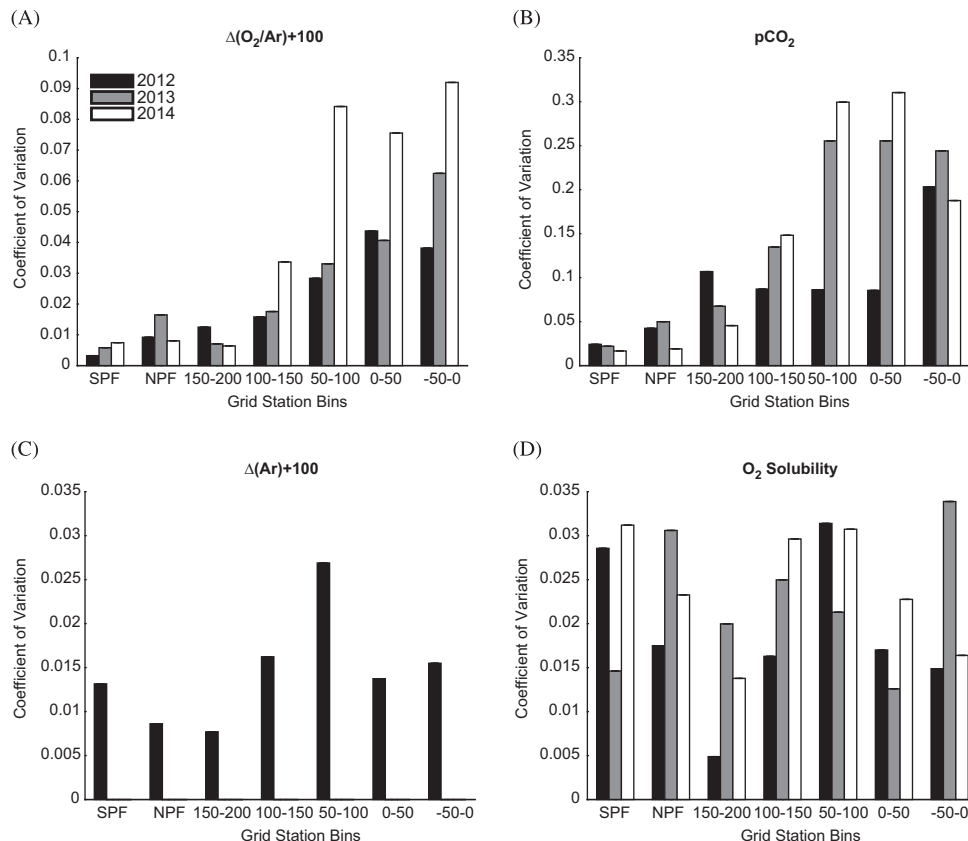
Fig. 4. Coefficient of variation in the Drake Passage north of the Polar Front (NPF) and south of the Polar Front (SPF) and 5 grid station bins (km offshore, see Fig. 1) arranged from offshore (left) to onshore (right) in 2012 (black), 2013 (gray) and 2014 (white) for (a) $\Delta(O_2/Ar)$, (b) $\Delta(pCO_2)$, (c) $\Delta(Ar)$, and (d) O_2 solubility.

$\Delta(pCO_2)$ is the most variable property in all bins and all years followed by $\Delta(O_2/Ar)$ (Fig. 4a and b). The difference in variability between $\Delta(pCO_2)$ and $\Delta(O_2/Ar)$ could be an effect of differential gas exchange whereby O_2 is more quickly driven to equilibrium than pCO_2. Additionally, $\Delta(pCO_2)$ variability is affected by both biological and physical processes, which may serve to enhance the magnitude of variability relative to $\Delta(O_2/Ar)$ that is driven by biology alone. $\Delta(pCO_2)$ and $\Delta(O_2/Ar)$ display onshore–offshore gradients in most years, with more variability in the onshore coastal region and less variability offshore. $\Delta(Ar)$ and O_2 solubility (approximately the same as Ar solubility) vary at similar magnitudes and show strong variability in the 50–100 km grid station bin where we observe a very strong north–south gradient due to active melting in the south (Fig. 4c and d). Temperature represents a more dominant control on O_2 solubility variability compared to salinity in both the LTER grid and Drake Passage (CV with SST held constant at mean is < 0.005, CV with SSS held constant at mean is 0.005–0.03).

We investigated the dominant scales of horizontal variability within the surface mixed layer using autocorrelation functions. A decorrelation length scale (DLS) was calculated by the e-folding length of the autocorrelation functions of $\Delta(O_2/Ar)$, $\Delta(Ar)$, $\Delta(pCO_2)$, salinity and temperature for each section and averaged yearly. The mean DLS for $\Delta(O_2/Ar)$, $\Delta(pCO_2)$, salinity and temperature was $\sim$4.5 km in the LTER grid region (Fig. 5). This length scale is comparable to the mean eddy diameter in the WAP which Martinson and McKee (2012) found to range from 3.2 to 5 km, consistent with an approximated Rossby radius of 4.8 ± 0.08 km. Differences between properties were not statistically significant in any year (1-way ANOVA $p > 0.05$). Additionally, there is no significant difference in DLS between years for any individual property analyzed here (1-way ANOVA $p > 0.05$). There is no apparent spatial trend in the scales of variability (e.g. DLS is not shorter in the near-coastal region than it is offshore).

Based on CV and DLS, $\Delta(O_2/Ar)$, $\Delta(pCO_2)$, $\Delta(Ar)$ salinity and temperature variability occurs over the same spatial scales but with differing magnitudes. The DLSs suggest that similar processes are controlling the distributions of the biological and physical properties in the WAP (in contrast to the Drake Passage, see below). However, the biology displays a greater magnitude of variability (CV) than physics likely owing to inherent internal bloom dynamics that allow more rapid changes of larger magnitude than physical processes (e.g. Doney et al., 2003; Mackas et al., 1985). Most importantly, the DLS indicates that LTER CTD-rosette station sampling every 20 km along gridlines and 100 km between gridlines is not sufficient to resolve the variability in the biological or physical systems of the WAP, and highlights the need for additional underway measurements (Schofield et al., 2010). Given

the short DLS, care should be taken when interpolating discrete data across this region.

3.4. Drake Passage

Overall in the Drake Passage biological O_2 saturations were closer to equilibrium than in the WAP region and physical oxygen (Ar) was steadily supersaturated (Table 1). Unlike in the WAP, $\Delta(Ar)$ was not correlated with temperature in the Drake Passage in 2012 (Fig. 6). However, given that it was the austral summer we might expect the Drake Passage to be warming overall. A 0.65 °C temperature increase during the residence time of Ar could account for the mean supersaturation observed ($1.5 \pm 0.8\%$) while a 1.47 °C warming could drive maximum observed supersaturations (3.4%). Comparing the 8-day average satellite-derived SST at the time of ship sampling to the previous 8-day average for the northbound transect during which we see the strong Ar supersaturations, the temperature change ranged from -1.7 °C to 2.5 °C with a mean near zero. Temperature changes may be contributing locally to physical oxygen saturations in the Drake Passage, but overall, given the lack of correlation and minimal mean temperature change over time, warming does not appear to be the main driver of the observed supersaturations.

Wind speeds are high through the Drake Passage and could be sustaining Ar supersaturations via bubble processes. If we again consider the bubble injection equation of Stanley et al. (2009) assuming a 2:1 ratio of bubble injection to exchange, an average mixed layer depth of 43 m from the January Argo climatology (Hosoda et al., 2010), an average wind speed of 10 m s^{-1} consistent with the weighted (Reuer et al., 2007) NCEP/NCAR Reanalysis surface wind speed history, and an average weighted piston velocity of 7.8 m d^{-1}, the total steady state balance of bubble processes and diffusive outgassing induces Ar supersaturation of 1.8%. This estimate accounts for the mean observed Ar supersaturation, and despite large uncertainty due to the number of assumptions and the 29% uncertainty of the bubble injection equation itself (Stanley et al., 2009), it confirms that bubbles are likely key drivers of the mean observed Ar supersaturation in the Drake Passage.

Pre-pressure corrected Ar supersaturation averaged 2.8% across the Drake Passage, thus decreasing atmospheric pressure prior to sampling accounted for about half of the raw measured physical oxygen supersaturation. One isolated region south of the PF during the southbound transect had small ($\sim -0.5\%$) pressure driven undersaturations. Pressure corrections are important before interpreting total oxygen data.

$\Delta(pCO_2)$ most strongly correlates with biological oxygen supersaturation in 2013 (Fig. 3, model II linear regression, slope -0.34,
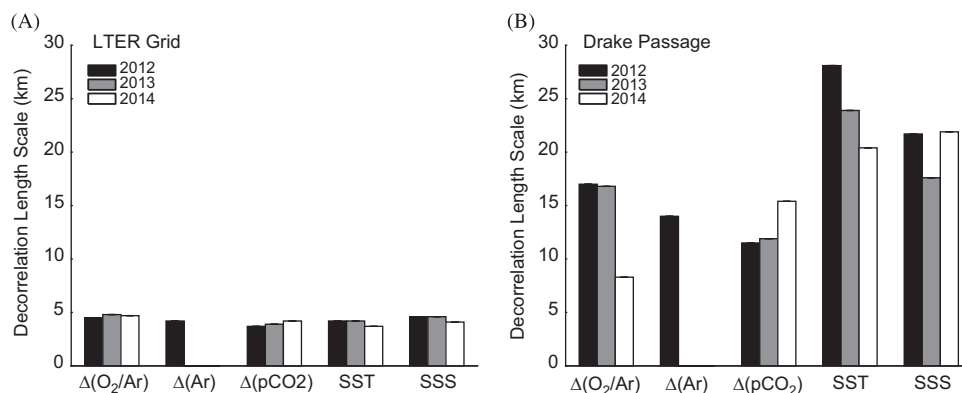

Fig. 5. Decorrelation length scale (km) determined by the e-folding length of the autocorrelation function for $\Delta(O_2/Ar)$, $\Delta(pCO_2)$, $\Delta(Ar)$, SST and SSS in: (a) the LTER grid region of the WAP and (b) the Drake Passage in 2012 (black), 2013 (gray) and 2014 (white).

$r^2 = 0.82$, $p < 0.0001$, $n = 582$). In 2014 the two gases are also correlated (slope -0.48, $r^2 = 0.44$, $p < 0.0001$, $n = 231$). These slopes are again shallower than that expected based on the theoretical photosynthetic quotient for saturation (~ -0.85, calculated as in 3.2.2 but with an oxygen saturation concentration of 321 μmol kg^{-1}
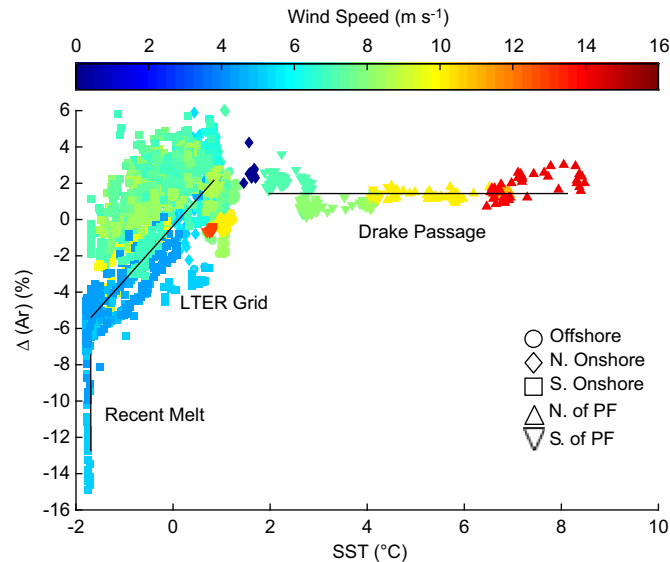

Fig. 6. Δ(Ar) vs. SST colored by weighted wind speed in the WAP and DP with symbol shape indicating region. Δ(Ar) uncertainty is $\pm 0.47\%$.

based on mean Drake Passage conditions). In 2013 Δ(O$_2$/Ar) and Δ(pCO$_2$) are coupled during the southbound leg in late December–early January ($r^2 = 0.89$, $p < 0.00001$, $n = 335$) but show no correlation in the northbound leg in February ($r^2 = 0.03$, $n = 247$) suggesting a decrease in rates of biological production between crossings. The two gases show no clear relationship in 2012. While Δ(O$_2$/Ar) is steadily near equilibrium across most of the Drake Passage in 2012, Δ(pCO$_2$) exhibits stronger variability north of the PF with supersaturations ranging from -12% to 11% (Fig. 7). The region just north of the PF is pCO$_2$ undersaturated in the southbound transect and supersaturated during the northbound transect a month later. While it is possible that this difference is a result of slightly different crossing longitudes and moving water masses, it also suggests a shift in the biological regime. The most likely undersaturating mechanism north of the Polar Front (PF) in the austral summer is biological drawdown (i.e. cooling, freshening and meltwater input are unlikely). It is possible that we document the end of the phytoplankton growing season during the January southbound crossing, and then the surface waters become pCO$_2$ supersaturated due to continued warming prior to the northbound crossing in February. This timing is consistent with other recent studies that show that most seasonal NCP occurs by early January (Munro et al., 2015; Weeding and Trull, 2014); this may also explain why we see stronger coupling between Δ(O$_2$/Ar) and Δ(pCO$_2$) in the southbound transect (late December–early January) compared to the northbound transect (early February) in 2013. Spatially, enhanced pCO$_2$ undersaturation is observed north of the PF relative to south of the front in the southbound transects (early January) in all three

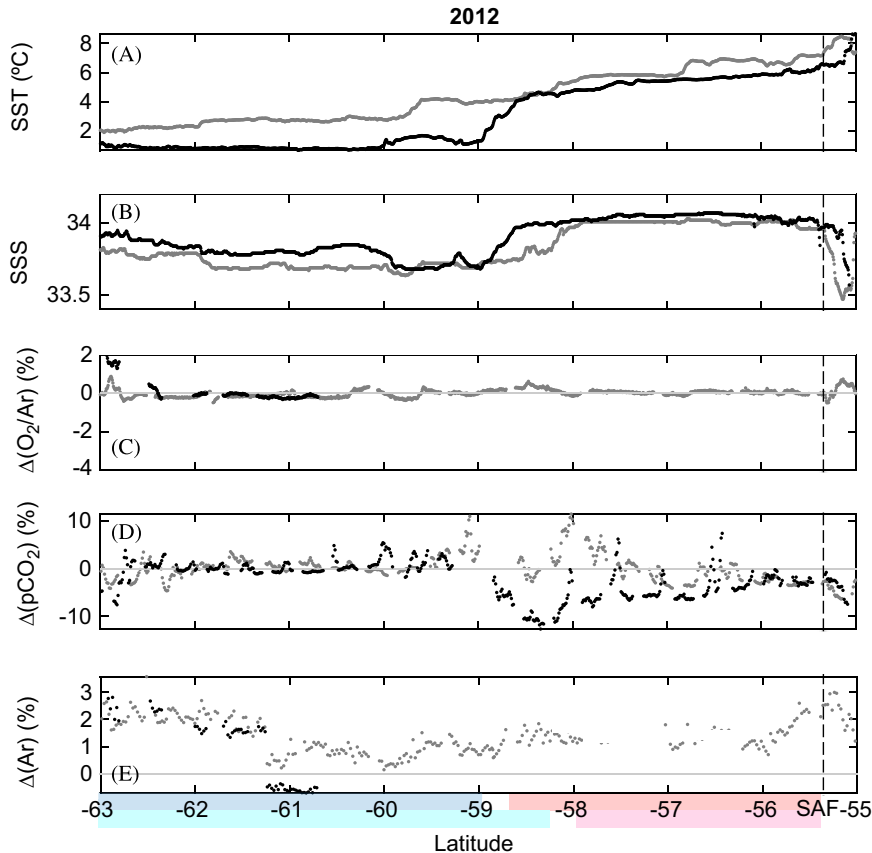**Fig. 7.** Underway measurements of (a) SST, (b) SSS, (c) Δ(O$_2$/Ar), (d) Δ(pCO$_2$) and (e) Δ(Ar) as a function of latitude across the Drake Passage in 2012. Black points are from the southbound crossing in early January and gray points are from the northbound crossing in early February. Colored bars indicate regions north and south of the Polar Front (NPF and SPF respectively) with SPF in blue shades and NPF in red shades for the southbound (top) and northbound (bottom) transects. The dotted line marks the approximate location of the Subantarctic Front (SAF). Δ(pCO$_2$) uncertainty is $\pm 0.45\%$, Δ(O$_2$/Ar) $\pm 0.3\%$, and Δ(Ar) $\pm 0.47\%$. (For interpretation of the references to color in this figure legend, the reader is referred to the web version of this article.)

years. In 2013 and 2014 $\Delta(p\text{CO}_2)$ drawdown is coincident with positive $\Delta(\text{O}_2/\text{Ar})$ suggesting elevated rates of biological production north compared to south of the PF consistent with previous NCP estimates for Drake Passage (Munro et al., 2015; Reuer et al., 2007). It is additionally worth noting that there is some interannual variability in $\Delta(\text{O}_2/\text{Ar})$ and $\Delta(p\text{CO}_2)$ with larger average deviations from equilibrium, and likely higher mean productivity in 2014 than in the previous two years with 2013 slightly more elevated than 2012. This is consistent with interannual variability in $\Delta(\text{O}_2/\text{Ar})$ and $\Delta(p\text{CO}_2)$ (and NCP (Eveleth et al., 2017b)) observed in the WAP and suggests the potential role of large-scale modes of climate variability (e.g. Southern Annular Mode, El Niño Southern Oscillation) influencing the entire area discussed herein (Li et al., in review).

Advection, mixing and entrainment presumably also affect $\Delta(\text{O}_2/\text{Ar})$ and $\Delta(p\text{CO}_2)$ in the Drake Passage (Jonsson et al., 2013; Munro et al., 2015). For example, in the northbound crossing in 2012 we observe $\Delta(p\text{CO}_2)$ supersaturation coincident with the location of the PF (Fig. 7d). Vertical mixing across the mixed layer boundary would likely lead to underestimation of biological activity for both O_2 and C-based methods. Jonsson et al. (2013) show that $\Delta(\text{O}_2/\text{Ar})$ based estimates in the Southern Ocean that assume steady-state and neglect budget terms for advection, mixing, and entrainment may underestimate NCP by 5–15%. During 2012, $\Delta(\text{O}_2/\text{Ar})$ (Fig. 7c) is steadily near equilibrium in the region of positive $\Delta(p\text{CO}_2)$ showing no indications of upwelling or entrainment of O_2 undersaturated water. This may indicate that any vertical mixing occurred several weeks prior to sampling so only $\Delta(p\text{CO}_2)$ retains memory of the event. The larger advection/entrainment signal for $\Delta(p\text{CO}_2)$ as compared to $\Delta(\text{O}_2/\text{Ar})$ is consistent with the analysis of Munro et al. (2015) who showed that C-budget estimates that neglect advection and entrainment terms underestimate NCP on average by 35% in Drake Passage, which is more than twice as large as biases noted for the O_2/Ar approach by Jonsson et al. (2013) for the open Southern Ocean.

Prior to analysis of spatial and temporal variability, the Drake Passage was divided into two regions (roughly north of the PF and south of the PF split at $-58.5°\text{S}$) so as to not capture the large SST and SSS changes across the PF in the coefficient of variation. On average, the magnitude of biological variability is lower in the Drake Passage than the WAP, with CV most comparable to the offshore region of the LTER grid (Fig. 4). $\Delta(\text{O}_2/\text{Ar})$ and $\Delta(p\text{CO}_2)$ both had slightly stronger variability north of the PF than south in 2013 and 2014. Salinity was also less variable in the Drake Passage compared to the WAP, presumably because of less active sea-ice and glacial meltwater input (data not shown). The strength of variability in O_2 solubility in the Drake compared closely with that in the WAP and was also driven more by temperature than salinity. $\Delta(\text{Ar})$ variability was within range of that observed in the less variable regions of the WAP and is of the same order of magnitude of $\Delta(\text{O}_2/\text{Ar})$ in the Drake Passage.

For autocorrelation analysis, data were pre-processed as in the LTER grid region using the northbound and southbound transects rather than gridlines. The DLS for all properties ($\Delta(\text{O}_2/\text{Ar})$, $\Delta(\text{Ar})$, $\Delta(p\text{CO}_2)$, temperature and salinity) is longer in the Drake Passage (defined here as between $55°\text{S}$ and $63°\text{S}$) than in the WAP and displays greater interannual variability (Fig. 5b). Additionally, $\Delta(\text{O}_2/\text{Ar})$ and $\Delta(p\text{CO}_2)$ have shorter DLSs than SST and SSS ($\sim$12 km compared to $\sim$20 km). $\Delta(\text{Ar})$ decorrelates at scales of $\sim$14 km. These scales are consistent with the 10–20 km heat flux DLSs found by Jiang et al. (2012) in the Drake Passage and the first baroclinic Rossby radius (as short as 10–20 km) in the region (Chelton et al., 1998). Biological properties exhibit higher magnitude variability than physical properties in the Drake Passage. This suggests some degree of decoupling of biological and physical processes in this region.

4. Conclusions

The LTER study region of the WAP is net autotrophic in January with positive $\Delta(\text{O}_2/\text{Ar})$ and negative $\Delta(p\text{CO}_2)$ overall and decreases in biological activity onshore to offshore. After accounting for atmospheric pressure history, Ar is near equilibrium in the mean driven by warming in the north and strong glacial and sea-ice meltwater input in the southern onshore grid region, but overall O_2 variability is biologically controlled. Importantly, the interactions of biological and physical saturation drivers in the marginal ice zone impede the ability to accurately interpret total O_2 signals in the WAP (e.g. from gliders, Bio-Argo floats). $\Delta(p\text{CO}_2)$ is also biologically driven but the net result of warming and freshening increases the mean supersaturation and melt may be enhancing variability. Spatial variability in the grid region overwhelms any diurnal cycle that may be expected for these gases. Biological signals (i.e., $p\text{CO}_2$ and $\Delta(\text{O}_2/\text{Ar})$) have a greater magnitude of variability than solubility and $\Delta(\text{Ar})$ but all decorrelate at spatial scales consistent with the Rossby radius ($\sim$4.5 km).

In contrast, in the Drake Passage $\Delta(\text{O}_2/\text{Ar})$ and $\Delta(p\text{CO}_2)$ were much nearer to equilibrium with respect to the atmosphere. We document differences in variability north and south of the PF with northward being slightly more variable biologically. DLS are longer in the Drake Passage than the WAP, but still consistent with the local Rossby radius ($\sim$10–20 km). $\Delta(\text{Ar})$ is relatively stable and supersaturated across the Drake Passage and is likely a result of large-scale seasonal warming and bubble injection due to high wind speeds. $p\text{CO}_2$ is biologically controlled in 2013 and 2014 but unrelated to $\Delta(\text{O}_2/\text{Ar})$ in 2012, when warming and other physical processes were more dominant.

Appendix A. Supplementary material

Supplementary data associated with this article can be found in the online version at http://dx.doi.org/10.1016/j.dsr2.2016.05.002.

References

Arrigo, K.R., van Dijken, G., Long, M., 2008. Coastal Southern Ocean: a strong anthropogenic CO_2 sink. Geophys. Res. Lett. 35 (21). http://dx.doi.org/10.1029/2008gl035624.

Beaird, N., Straneo, F., Jenkins, W., 2015. Spreading of Greenland meltwaters in the ocean revealed by noble gases. Geophys. Res. Lett. 42 (18), 7705–7713. http://dx.doi.org/10.1002/2015gl065003.

Broecker, W.S., Peng, T.H., 1974. Gas-exchange rates between air and sea. Tellus 26 (1–2), 21–35.

Caldeira, K., Duffy, P.B., 2000. The role of the Southern Ocean in uptake and storage of anthropogenic carbon dioxide. Science 287 (5453), 620–622. http://dx.doi.org/10.1126/science.287.5453.620.

Carrillo, C.J., Smith, R.C., Karl, D.M., 2004. Processes regulating oxygen and carbon dioxide in surface waters west of the Antarctic Peninsula. Mar. Chem. 84 (3–4), 161–179. http://dx.doi.org/10.1016/j.marchem.2003.07.004.

Cassar, N., Barnett, B.A., Bender, M.L., Kaiser, J., Hamme, R.C., Tilbrook, B., 2009. Continuous High-frequency dissolved O-2/Ar measurements by equilibrator inlet mass spectrometry. Anal. Chem. 81 (5), 1855–1864. http://dx.doi.org/10.1021/Ac802300u.

Cassar, N., DiFiore, P.J., Barnett, B.A., Bender, M.L., Bowie, A.R., Tilbrook, B., Petrou, K., Westwood, K.J., Wright, S.W., Lefevre, D., 2011. The influence of iron and light on net community production in the Subantarctic and Polar Frontal Zones. Biogeosciences 8 (2), 227–237. http://dx.doi.org/10.5194/Bg-8-227-2011.

Castro-Morales, K., Cassar, N., Shoosmith, D.R., Kaiser, J., 2013. Biological production in the Bellingshausen Sea from oxygen-to-argon ratios and oxygen triple isotopes. Biogeosciences 10 (4), 2273–2291. http://dx.doi.org/10.5194/Bg-10-2273-2013.

Chelton, D.B., DeSzoeke, R.A., Schlax, M.G., El Naggar, K., Siwertz, N., 1998. Geographical variability of the first baroclinic Rossby radius of deformation. J. Phys. Oceanogr. 28 (3), 433–460. doi:10.1175/1520-0485(1998)028 < 0433: Gvotfb > 2.0.Co;2.

Doney, S.C., Glover, D.M., McCue, S.J., Fuentes, M., 2003. Mesoscale variability of Sea-viewing Wide Field-of-view Sensor (SeaWiFS) satellite ocean color: global patterns and spatial scales. J. Geophys. Res.-Oceans 108 (C2). http://dxdoi.org/10.1029/2001jc000843.

Eveleth, R., Timmermans, M.L., Cassar, N., 2014. Physical and biological controls on oxygen saturation variability in the upper Arctic Ocean. J. Geophys. Res.-Oceans 119 (11), 7420–7432. http://dx.doi.org/10.1002/2014jc009816.

Eveleth, R., Cassar, N., Sherrell, R.M., Ducklow, H., Meredith, M., Venables, H.J., Lin, Y., Li, Z., 2017b. Ice melt influence on summertime net community production along the Western Antarctic Peninsula. Deep Sea Research Part II: Topical Studies in Oceanography 139, 89–102. http://dx.doi.org/10.1016/j.dsr2.2016.07.016.

Garcia, H.E., Gordon, L.I., 1992. Oxygen solubility in seawater – better fitting equations. Limnol. Oceanogr. 37 (6), 1307–1312.

Hamme, R.C., et al., 2012. Dissolved O-2/Ar and other methods reveal rapid changes in productivity during a Lagrangian experiment in the Southern Ocean. J. Geophys. Res.-Oceans, 117. http://dx.doi.org/10.1029/2011jc007046.

Hamme, R.C., Emerson, S.R., 2002. Mechanisms controlling the global oceanic distribution of the inert gases argon, nitrogen and neon. Geophys. Res. Lett. 29 (23). http://dx.doi.org/10.1029/2002gl015273.

Hamme, R.C., Emerson, S.R., 2004. The solubility of neon, nitrogen and argon in distilled water and seawater. Deep.-Sea Res. Part I 51 (11), 1517–1528. http://dx.doi.org/10.1016/J.Dsr.2004.06.009.

Hamme, R.C., Emerson, S.R., 2006. Constraining bubble dynamics and mixing with dissolved gases: implications for productivity measurements by oxygen mass balance. J. Mar. Res. 64 (1), 73–95. http://dx.doi.org/10.1357/002224006776412322.

Hauri, C., Doney, S.C., Takahashi, T., Erickson, M., Jiang, G., Ducklow, H.W., 2015. Two decades of inorganic carbon dynamics along the Western Antarctic Peninsula. Biogeosci. Discuss. 12 (9), 6929–6969. http://dx.doi.org/10.5194/bgd-12-6929-2015.

Hood, E.M., 1998. Characterization of Air–sea Gas Exchange Processes and Dissolved Gas/ice Interactions Using Noble Gases (Ph.D. thesis). MIT/WHOI.

Hosoda, S., Ohira, T., Sato, K., Suga, T., 2010. Improved description of global mixed-layer depth using Argo profiling floats. J. Oceanogr. 66 (6), 773–787. http://dx.doi.org/10.1007/S10872-010-0063-3.

Huang, K., Ducklow, H., Vernet, M., Cassar, N., Bender, M.L., 2012. Export production and its regulating factors in the West Antarctica Peninsula region of the Southern Ocean. Glob. Biogeochem. Cycles, 26. http://dx.doi.org/10.1029/2010gb004028.

Jiang, C.L., Gille, S.T., Sprintall, J., Yoshimura, K., Kanamitsu, M., 2012. Spatial variation in turbulent heat fluxes in Drake Passage. J. Clim. 25 (5), 1470–1488. http://dx.doi.org/10.1175/2011jcli4071.1.

Jonsson, B.F., Doney, S.C., Dunne, J., Bender, M., 2013. Evaluation of the Southern Ocean O-2/Ar-based NCP estimates in a model framework. J. Geophys. Res.-Biogeosci. 118 (2), 385–399. http://dx.doi.org/10.1002/Jgrg.20032.

Juranek, L.W., Hamme, R.C., Kaiser, J., Wanninkhof, R., Quay, P.D., 2010. Evidence of O-2 consumption in underway seawater lines: Implications for air-sea O-2 and CO2 fluxes. Geophys. Res. Lett., 37. http://dx.doi.org/10.1029/2009gl040423.

Kavanaugh, M.T., Abdala, F.N., Ducklow, H., Glover, D., Fraser, W., Martinson, D., Stammerjohn, S., Schofield, O., Doney, S.C., 2015. Effect of continental shelf canyons on phytoplankton biomass and community composition along the western Antarctic Peninsula. Mar. Ecol. Prog. Ser. 524, 11–26. http://dx.doi.org/10.3354/Meps11189.

Li Z., Cassar N., Huang K., Ducklow H., Schofield O., Interannual variability in net community production at the Western Antarctic Peninsula region (1997-2014), J. Geophys. Res.-Oceans, in review.

Loose, B., Jenkins, W.J., 2014. The five stable nobel gases are sensitive unambiguous tracers of glacial meltwater. Geophys. Res. Lett., 41. http://dx.doi.org/10.1002/2013GL058804.

Mackas, D.L., Denman, K.L., Abbott, M.R., 1985. Plankton patchiness – biology in the physical vernacular. Bull. Mar. Sci. 37 (2), 652–674.

Martin, P., et al., 2013. Iron fertilization enhanced net community production but not downward particle flux during the Southern Ocean iron fertilization experiment LOHAFEX. Glob. Biogeochem. Cycles 27 (3), 871–881. http://dx.doi.org/10.1002/gbc.20077.

Martinson, D.G., McKee, D.C., 2012. Transport of warm Upper Circumpolar Deep Water onto the western Antarctic Peninsula continental shelf. Ocean Sci. 8 (4), 433–442. http://dx.doi.org/10.5194/Os-8-433-2012.

Martinson, D.G., Stammerjohn, S.E., Iannuzzi, R.A., Smith, R.C., Vernet, M., 2008. Western Antarctic Peninsula physical oceanography and spatio-temporal variability. Deep.-Sea Res. Part II 55 (18–19), 1964–1987. http://dx.doi.org/10.1016/J.Dsr2.2008.04.038.

Meredith, M.P., Stammerjohn, S., Venables, H.J., Ducklow, H., Martinson, D., Iannuzzi, R., Leng, M.J., Melchoir van Wessem, J., Reijmer, C.H., Barrand, N.E., 2017. Changing distributions of sea ice melt and meteoric water west of the Antarctic Peninsula. Deep-Sea Res. Part II: Top. Stud. Oceanogr. 139, 40–57. http://dx.doi.org/10.1016/j.dsr2.2016.04.019.

Meredith, M.P., Venables, H.J., Clarke, A., Ducklow, H.W., Erickson, M., Leng, M.J., Lenaerts, J.T.M., van den Broeke, M.R., 2013. The Freshwater System West of the Antarctic Peninsula: spatial and temporal changes. J. Clim. 26 (5), 1669–1684. http://dx.doi.org/10.1175/Jcli-D-12-00246.1.

Mu, L., Stammerjohn, S., Lowry, K., Yager, P., 2014. Spatial variability of surface pCO2 and air–sea CO2 flux in the Amundsen Sea Polynya, Antarctica. Elem.: Sci. Anthropol. 2 (1), 000036.

Munro, D.R., Lovenduski, N.S., Stephens, B.B., Newberger, T., Arrigo, K.R., Takahashi, T., Quay, P.D., Sprintall, J., Freeman, N., Sweeney, C., 2015. Estimates of net community production determined from time series observations (2002–2011) of nutrients, dissolved inorganic carbon, and surface ocean pCO2 in drake passage. Deep.-Sea Res. Part II: Top. Stud. Oceanogr. (0). http://dxdoi.org/10.1016/j.dsr2.2014.12.014

Reuer, M.K., Barnett, B.A., Bender, M.L., Falkowski, P.G., Hendricks, M.B., 2007. New estimates of Southern Ocean biological production rates from O-2/Ar ratios and the triple isotope composition of O-2. Deep.-Sea Res. Part I 54 (6), 951–974. http://dx.doi.org/10.1016/J.Dsr.2007.02.007.

Sarmiento, J.L., Gruber, N., 2006. Ocean Biogeochemical Dynamics, xii. Princeton University Press, Princeton, NJ, p. 503 (508 pp. of plates).

Schofield, O., et al., 2013. Penguin biogeography along the West Antarctic Peninsula testing the canyon hypothesis with palmer LTER observations. Oceanography 26 (3), 204–206.

Schofield, O., Ducklow, H.W., Martinson, D.G., Meredith, M.P., Moline, M.A., Fraser, W.R., 2010. How Do polar marine ecosystems respond to rapid climate change? Science 328 (5985), 1520–1523. http://dx.doi.org/10.1126/Science.1185779.

Shadwick, E.H., Tilbrook, B., Cassar, N., Trull, T.W., Rintoul, S.R., 2015. Summertime physical and biological controls on O-2 and CO2 in the Australian Sector of the Southern Ocean. J. Mar. Syst. 147, 21–28. http://dx.doi.org/10.1016/j.jmarsys.2013.12.008.

Stanley, R.H.R., Jenkins, W.J., Doney, S.C., 2006. Quantifying seasonal air-sea gas exchange processes using noble gas time-series: a design experiment. J. Mar. Res. 64 (2), 267–295. http://dx.doi.org/10.1357/002224006777606452.

Stanley, R.H.R., Jenkins, W.J., Lott, D.E., Doney, S.C., 2009. Noble gas constraints on air-sea gas exchange and bubble fluxes. J. Geophys. Res.-Oceanogr., 114. http://dx.doi.org/10.1029/2009jc005396.

Stanley, R.H.R., Kirkpatrick, J.B., Cassar, N., Barnett, B.A., Bender, M.L., 2010. Net community production and gross primary production rates in the western equatorial Pacific. Glob. Biogeochem. Cycles 24. http://dxdoi.org/10.1029/2009gb003651.

Takahashi, T., Olafsson, J., Goddard, J.G., Chipman, D.W., Sutherland, S.C., 1993. Seasonal-variation of CO2 and nutrients in the high-latitude surface oceans – a comparative-study. Glob. Biogeochem. Cycles 7 (4), 843–878. http://dx.doi.org/10.1029/93gb02263.

Top, Z., Martin, S., Becker, P., 1988. A laboratory study of dissolved noble-gas anomaly due to ice formation. Geophys. Res. Lett. 15 (8), 796–799. http://dx.doi.org/10.1029/Gl015i008p00796.

Tortell, P.D., Asher, E.C., Ducklow, H.W., Goldman, J.A.L., Dacey, J.W.H., Grzymski, J.J., Young, J.N., Kranz, S.A., Bernard, K.S., Morel, F.M.M., 2014. Metabolic balance of coastal Antarctic waters revealed by autonomous pCO2 and ΔO2/Ar measurements. Geophys. Res. Lett. 41 (19). http://dx.doi.org/10.1002/2014GL061266.

Tortell, P.D., Bittig, H.C., Körtzinger, A., Jones, E.M., Hoppema, M., 2015. Biological and physical controls on N2, O2 and CO2 distributions in contrasting Southern Ocean surface waters. Glob. Biogeochem. Cycles. http://dx.doi.org/10.1002/2014GB004975.

Tortell, P.D., Long, M.C., 2009. Spatial and temporal variability of biogenic gases during the Southern Ocean spring bloom. Geophys. Res. Lett., 36. http://dx.doi.org/10.1029/2008gl035819.

Weeding, B., Trull, T.W., 2014. Hourly oxygen and total gas tension measurements at the Southern Ocean Time Series site reveal winter ventilation and spring net community production. J. Geophys. Res.-Oceanogr. 119 (1), 348–358. http://dx.doi.org/10.1002/2013jc009302.

Zhou, J.Y., Delille, B., Eicken, H., Vancoppenolle, M., Brabant, F., Carnat, G., Geilfus, N.X., Papakyriakou, T., Heinesch, B., Tison, J.L., 2013. Physical and biogeochemical properties in landfast sea ice (Barrow, Alaska): insights on brine and gas dynamics across seasons. J. Geophys. Res.-Oceanogr. 118 (6), 3172–3189. http://dx.doi.org/10.1002/jgrc.20232.